Research Square

Preprints are preliminary reports that have not undergone peer review.
They should not be considered conclusive, used to inform clinical practice,
or referenced by the media as validated information.

Investigating Mode I Fracture of Ti-6Al-4V Lattice Structure Fabricated by Laser Powder Bed Fusion

Bahman Paygozar

bpaygozar@etu.edu.tr

TOBB University of Economics and Technology

Recep M. Gorguluarslan

TOBB University of Economics and Technology

Nazim Babacan

Sivas University of Science and Technology

Research Article

Keywords: Laser powder bed fusion, Mode I fracture, Lattice structure, Extended finite element method, Equivalent solid material model

Posted Date: April 9th, 2026

DOI: https://doi.org/10.21203/rs.3.rs-9360674/v1

License: This work is licensed under a Creative Commons Attribution 4.0 International License.
Read Full License

Additional Declarations: No competing interests reported.

Investigating Mode I Fracture of Ti-6Al-4V Lattice Structure Fabricated by Laser Powder Bed Fusion

Abstract: This study experimentally and numerically investigates the mode I fracture behavior of near-isotropic Face- and Simple-Center Cubic (FSCC) lattice structures fabricated from Ti-6Al-4V using Laser Powder Bed Fusion (PBF-LB/M). Single-edge notched bending (SENB) specimens were subjected to quasi-static three-point bending tests, and scanning electron microscopy (SEM) was conducted on the fracture surfaces to analyze crack propagation paths and crack planes within the struts. To efficiently predict damage initiation and evolution without the high computational cost of explicitly modeling complex lattice architectures, an equivalent solid material model (ESMM) was employed in conjunction with the eXtended Finite Element Method (XFEM). The maximum principal stress and fracture energy power-law criteria were utilized to simulate damage initiation and evolution in three-dimensional numerical simulations. By applying a common calibration factor to the base material properties, the integrated ESMM-XFEM approach demonstrated good agreement with the experimental load-displacement responses, exhibiting minimal differences of 2.2% and 7.9% for peak load and stiffness, respectively. These findings validate the consistent mode I fracture resistance of the PBF-LB/M-fabricated Ti-6Al-4V FSCC lattice, establishing the ESMM-XFEM framework as an efficient tool for evaluating damage-tolerant lattice components.

Keywords: Laser powder bed fusion, Mode I fracture, Lattice structure, Extended finite element method, Equivalent solid material model.

Highlights:

- Implementing the XFEM technique in simulating mode I fracture behaviors.
- Simulating fracture behavior of FSCC lattice specimens using ESMM.
- Modelling crack propagation in additively manufactured Ti-6Al-V lattice specimens.
- Investigating the fracture surfaces using SEM analysis.

1. Introduction

Lattice or cellular solids are formed by the periodical arrangement of a specific pattern of lattice cells, and the struts of lattice cells are straight rods that have a regular cell size and shape. Lattice structures feature diverse cell geometries and higher porosity than traditional foam materials [1]. They not only have the characteristics of light weight and high specific strength but also exhibit appropriate performance in multifunctional applications, such as impact resistance, heat insulation, and electromagnetic wave absorption [2, 3].

However, lattice structures are difficult to fabricate with traditional manufacturing methods due to their highly complex spatial architecture. The rapid development of additive manufacturing (AM) technology in recent years has enabled the widespread use of lattice materials. AM technology is an advanced manufacturing method based on the discrete-cumulative principle, representing a bottom-up approach compared to traditional material removal technologies [4]. This technology enables the production of complex three-dimensional lattice structures with reduced time and production costs [5, 6]. One practical AM technique for fabricating metallic components is laser powder bed fusion (PBF-LB/M), which can produce components from various materials and has a wide range of applications across various industries [7-9].

Mazur et al. [10] utilized the PBF-LB/M technique to investigate the effects of topological configuration, strut dimensions, and the number of unit cells on structural mechanical properties under compressive load. It was found that PBF-LB/M technology can produce complex lattice structures with minor geometric defects and high structural integrity. In addition to the geometric complexity achievable with AM, the diversity of compatible materials (e.g., Ti-6Al-4V and 316L stainless steel) is another major advantage of this technique. For instance, Ti-6Al-4V has superior fatigue resistance, a high strength-to-weight ratio, and excellent corrosion resistance [11-13], resulting in exceptional mechanical properties for the component made from it [14, 15]. Consequently, Ti-6Al-4V is considered a promising candidate for the fabrication of lattice structures [16]. For this reason, lattice structures made of Ti-6Al-4V are widely used in automotive [17, 18], aerospace [19, 20], and biomedical [21, 22] applications.

Many scholars have conducted mechanical property tests by designing diverse lattice structures with different unit configurations and relative densities to investigate their mechanical and fracture behaviors. The mechanical properties of additive-manufactured metallic lattice structures have been intensively studied, including the quasi-static [16, 23-26] and dynamic [27-29] compressive properties, fatigue behavior [30, 31], flexural performance [32], and shear properties [23, 32]. Among various strut-based lattice cells, the face- and simple-centered cubic (FSCC) lattice was shown to have near-isotropic elastic properties when all strut members have equal diameters [33]. Since this cell is based on a face-centered cubic (FCC) cell, with the placement of vertical and horizontal struts at the face-centers being referred to as simple-centered cubic (SCC), there are no overhang issues during AM because the center points are inherently self-supporting. Moreover, because struts are centrally located, they are expected to have balanced effective properties in every direction, leading to a nearly isotropic lattice cell [33]. It was also shown that FSCC lattice specimens can be fabricated by PBF-LB/M from SS4130 material without any overhang issue and exhibit superior energy absorption metrics among various lattice types under quasi-static compression tests [34]. Furthermore, since the struts connecting the surface centers delay fracture from these typically weak points, properties such as fracture load and toughness are predicted to be high under fracture tests as observed from FSCC specimens fabricated by material extrusion using PLA [35, 36].

Despite these advantages, the literature lacks any investigation of Mode I fracture in PBF-LB/M-fabricated FSCC lattice structures made of Ti-6Al-4V alloy. In highly anisotropic lattices, cracks tend to propagate rapidly along specific structurally weak planes. In contrast, the nearly isotropic elastic properties of the FSCC lattice imply a more uniform resistance to crack growth, enhancing overall damage tolerance. This makes the FSCC lattice highly promising for damage-tolerant applications subjected to unpredictable, multidirectional loading environments where fracture is likely to occur, such as orthopedic implants and aerospace structural nodes. The main goal of this study is to reveal the advantages of the Ti-6Al-4V FSCC cell in fracture tests using experimental and numerical investigations. Additionally, it is observed that the fracture behavior, especially the crack propagation, of Ti-6Al-4V FSCC lattice material fabricated by the PBF-LB/M has not been investigated through combined experimental and numerical investigations. The only relevant study performed by Daynes et al. [37] utilized beam elements in a conventional finite element method to simulate the crack propagation by incrementally removing the symmetry boundary condition on each octet-truss unit cell along the crack plane as the crack propagated alongside the sample width. However,

this approach needs high computational costs and few number of iterations used during mesh refinement, thereby reducing the accuracy of the numerical results. To address the gap, mode I fracture tests of Ti-6Al-4V FSCC samples were conducted, and the crack propagation and fracture behavior (e.g., fracture load) under mode I fracture loading were investigated. Furthermore, to overcome the high computational cost of explicitly modeling complex microstructures, fracture simulations were performed using the extended finite element method (XFEM) coupled with an equivalent solid material model (ESMM). After calibrating the base material properties of Ti-6Al-4V, the ESMM approach was employed to facilitate the numerical fracture analyses of the lattice specimens using the XFEM technique.

2. Experimental study

2.1. Manufacturing of the specimens

The single-edge notch bending (SENB) specimens were manufactured for mode I tests, comprising 28×6×3 cubic FSCC lattice cells of 0.9 mm-thick strut diameter and 4 mm unit cell edge length (corresponding to a relative density of 33.72%). The specimens were manufactured in dimensions of 112×24×12 mm, as shown in Fig. 1. Three samples were built using a PBF-LB/M machine (ENA VISION 130, Ermaksan, Türkiye) that is equipped with a modulated 500 W fiber laser. The powder material feedstock Ti6Al4V, provided by Ermaksan company, was used in this study. The utilized process parameters while fabricating the SENB specimens are listed in Table 1. All the samples were built in a protective argon atmosphere. A 3 mm-high support structure was automatically generated using Magics (Materialise, Belgium) to facilitate the removal of the specimens from the build platform after fabrication. The fabricated specimens and the corresponding support structures used during manufacturing are shown in Supplementary File 1.

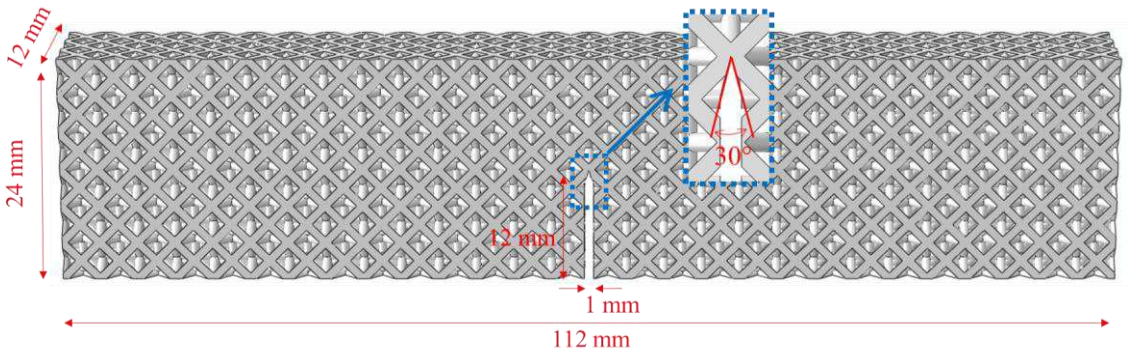


Fig. 1. Dimensions of the SENB specimen with FSCC lattice.

Table 1. Process parameters used for fabrication.

Process parameters	Quantity
Laser power [W]	240
Laser spot diameter [µm]	85
Layer thickness [µm]	30
Hatch distance [µm]	100
Scanning speed [mm/s]	1000
Scanning strategy	Chess (4.83 mm)
Support type	Cones
Atmosphere	Argon
Ti-6Al-4V Powder (ERMAK Gd5)	10-45 µm

2.2. Testing procedure

Three-point (3P) bending experiments were conducted for the mode I fracture of three fabricated lattice SENB specimens in a universal testing machine (Instron 600 LX, USA). A loading speed of 0.5 mm/min was applied, and 3P bending fixtures were utilized, as shown in Fig. 2. The testing procedure was recorded with a Canon EOS D250 standard camera.

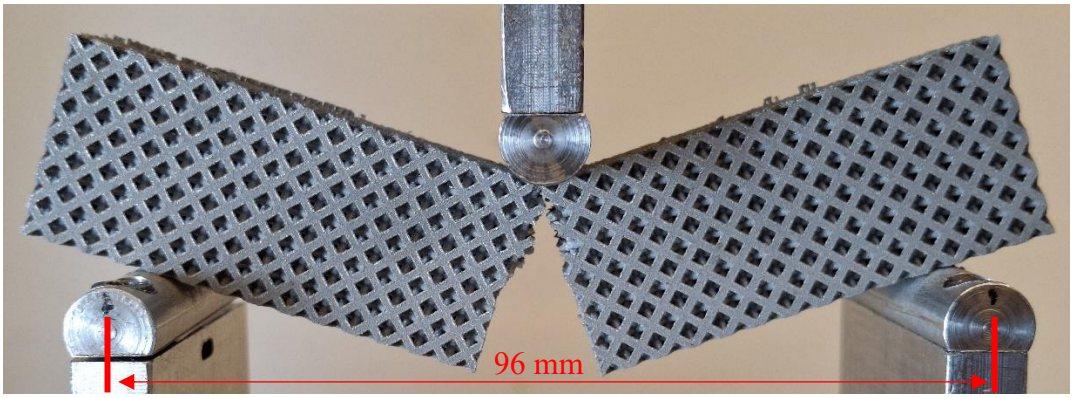


Fig. 2. A SENB lattice specimen under Mode I 3P-bending testing.

3. Numerical Study

3.1. Equivalent Solid Material Model (ESMM)

The ESMM is a practical technique used to simplify the numerical analyses of complex configurations like lattice structures, including several struts located in different directions. In this regard, the fracture simulations of the FSCC lattice structure were not investigated via detailed models because there are too many lattice cells in the lattice SENB specimens; hence, there would be high computational costs, thereby making any detailed analyses very difficult, if not impossible. Additionally, the complexity of the geometry of the lattice specimens is magnified by the high number of struts in use and the connection points of the struts together, which leads to convergence issues in fracture simulations. Hence, the use of the ESMM and working with equivalent solid specimens made the analyses computationally cost-effective and reduced the convergence issues.

A similar equivalent modeling approach to the ones implemented in the literature [38, 39] was implemented in this study to predict the equivalent material and fracture properties of the FSCC lattice specimens by calibrating them based on experimental results. The implemented methodology is shown in Fig. 3. As depicted in the figure, the response curve of the equivalent solid model is matched with the response curve of the fracture test of the lattice specimen to calibrate the effective material and fracture properties. Thus, the lattice can be represented by the equivalent solid model.

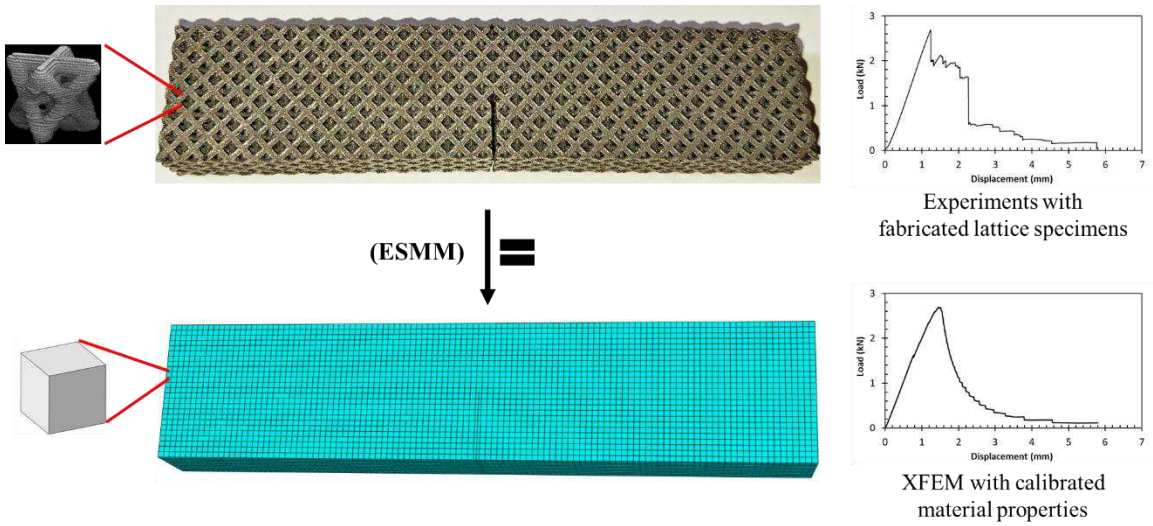


Fig. 3. Illustration of the implemented ESMM technique.

3.2. Extended Finite Element Method (XFEM)

To simulate the fracture, the XFEM technique was used in this study. It is a numerical approach capable of dealing with discontinuities like cracks, thereby facilitating the simulation of material fracture behavior (e.g., crack propagation) [40, 41]. The XFEM enables the crack to propagate through the element interior by incorporating enrichment functions into the conventional FE method. It also predicts crack propagation in additively manufactured parts [41, 42]. The enrichment functions in XFEM facilitate displacement jumps across crack faces and model the singularity at the crack tip [43]. The discretized displacement field, u^h in XFEM [44], is defined by

$$u_{(x)}^h = \sum_{i\epsilon N} N_i(x)\left[u_i + H(x)a_i + \sum_{j=1}^{4} F_j(x)b_i^j\right] \quad (1)$$

where N_i and u_i are the blending function and the nodal displacement vector, respectively. $H(x)a_i$ indicates a Heaviside enrichment, and $\sum_{j=1}^{4} F_j(x)b_i^j$ shows crack tip enrichment. The superscripts *i* and *j* demonstrate the node number and the enrichment function's number at the crack front, respectively. Also, $H(x)$ indicates the Heaviside distribution, a_i reflects the enriched nodal degree of freedoms for the elements cut through the crack (i.e., jump discontinuity). $F_j(x)$ and b_i^j are respectively referred to as the crack tip asymptotic function and the crack tip enriched nodal degree of freedom [45].

The crack initiation and propagation processes in XFEM were modeled by a cohesive traction-separation law [46, 47]. To use the linear type of traction-separation law, the maximum principal stress (MaxPS) criterion was selected in this study to model the crack initiation [48]. According to this criterion, when the maximum principal stress (σ_p) experienced in an element reaches the ultimate strength (σ_u) of the material, the material starts to fail from that element. The failure equation is given by.

$$\frac{\sigma_p}{\sigma_u} = 1 \quad (2)$$

Fracture energy power-law criteria in 3D versions can be used to model crack propagation through damage evolution [47, 49].

$$\left\{\frac{G_n}{G_n^C}\right\} + \left\{\frac{G_s}{G_s^C}\right\} + \left\{\frac{G_t}{G_t^C}\right\} = 1 \quad (3)$$

where, G_n, G_s, and G_t are strain energy release rates (i.e., fracture energies) in normal, first, and second shear directions concerning the interface, respectively. Superscript *C*, added to the

previous parameters, reflects their critical values. Considering the experimental investigations of this study, i.e., dealing with either pure Mode I, only the first term of the equation above will be active on the left-hand side. It is worth noting that the critical mode I fracture energy can be found using Eq. (4) and mode I fracture toughness. The symbols E and ν denote the material's Young's modulus and Poisson's ratio, respectively.

$$G_n^C = G_{Ic} = \frac{K_I^2(1-\nu^2)}{E} \quad (4)$$

3.3. Finite element models

The mode I SENB specimen was modeled with eight-node brick elements (signified by C3D8 in ABAQUS) to build the equivalent finite element model used in the XFEM, as shown in Fig.3. The 3P-bending fixture's rigid rollers of 5 mm in radius were modeled as an analytical rigid solid for mode I specimens. All the DOFs of the rollers at the bottom and all the DOFs of the roller at the top, except for displacement in the loading direction, were constrained. A general contact (standard) algorithm was introduced to the structures, which comprise both normal and tangential behaviors, with a friction coefficient of 0.3.

3.4. Calibration of material properties

In the calibration process of the ESMM, the mechanical and fracture properties of Ti-6Al-4V, listed in Table 2 [50], were initially used. The simulation results were compared with the experimental results to examine the accuracy of the results and calibrate the material properties to match the XFEM results with the experimental results.

Table 2. The material properties of Ti-6Al-4V standard solid specimens fabricated by PBF-LB/M used in the XFEM analyses as a starting point [50].

E [GPa]	σ_y [MPa]	ν	K_{IC} [$MPa\sqrt{m}$]
117	1140	0.34	45

Given Fig. 4, the following steps were implemented as the solution procedure:

a. Generating the equivalent solid models of lattice specimens. They were used as the equivalent solid models in the XFEM analyses when implementing the ESMM approach.
b. Utilizing Ti-6Al-4V material properties (Table 2) as the starting point in the XFEM analyses of mode I fracture using the ESMM approach.
c. Starting the XFEM simulations of the equivalent solid.
d. Calibrating the material properties by comparing the XFEM results with the experimental results of the lattice specimens for mode I fracture tests.
e. Extracting the last calibrated material properties. The final calibrated material properties were selected when a reasonably small difference between the experimental and numerical stiffness and peak load values was reached.

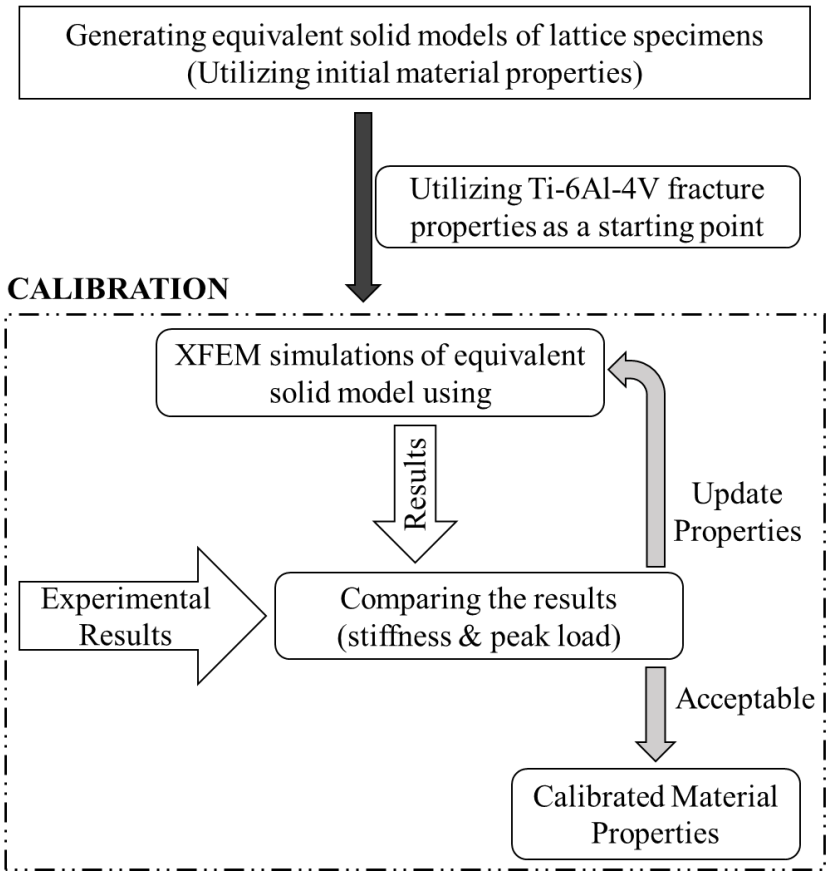


Fig. 4. Flowchart of the implemented calibration procedure.

4. Results and discussion

4.1. Experimental results

After conducting the 3P-bending tests on the SENB lattice specimens, the load-displacement curves were extracted. Then, the mechanical properties of the specimens (i.e., peak load and stiffness) were obtained from the load-displacement responses, listed in Table 3. The lower amounts of percentage ratios (i.e., the standard deviation value divided by the average value) approve the suitability and repeatability of the tests.

Table 3. Experimental data obtained from Mode 3P-bending tests.

Property	Sample 1	Sample 2	Sample 3	Avg.	St. Dev.	Ratio (%)
Peak Load [N]	2693	2878	2669	2746.67	114.37	4.2
Stiffness [N/mm]	2441	2548	2390	2459.67	80.64	3.3

Additionally, several photos were taken during the fracture of one selected specimen (sample 1) imposed by the 3P-bending loading. The crack propagation at different stages of the loading, and their corresponding points on the load-displacement curves, are shown in Fig. 5.

It is seen that the loading rises up to point a1 linearly because of elastic behavior and continues up to point a2 almost in the same trend. At point a2, the crack starts to propagate diagonally, which is not expected due to the nature of mode I loading. A sudden drop in the experienced load during the segment a2-a3, is because of internal struts failure, at which the sharp crack tip was located. The small fluctuations in the loading history between points a3 and a4 reflect the crack growth in the struts and the creation of different fracture planes in the affected struts during the crack growth. The creation of different fracture planes in the fracture surface of a failed strut was also investigated using SEM images, as later shown in Figs. 9(a) and (b). The second sudden drop occurs in the segment a4-a5 owing to the complete failure of the second row of the struts inside the lattice structure. After point a5, the crack grows rapidly since the structure has lost its strength to withstand the crack propagation. At point a6, the load tolerated by the structure goes below 10% of the peak load, followed by a complete separation of the specimen after 1.2mm further displacement of the puncher (top roller).

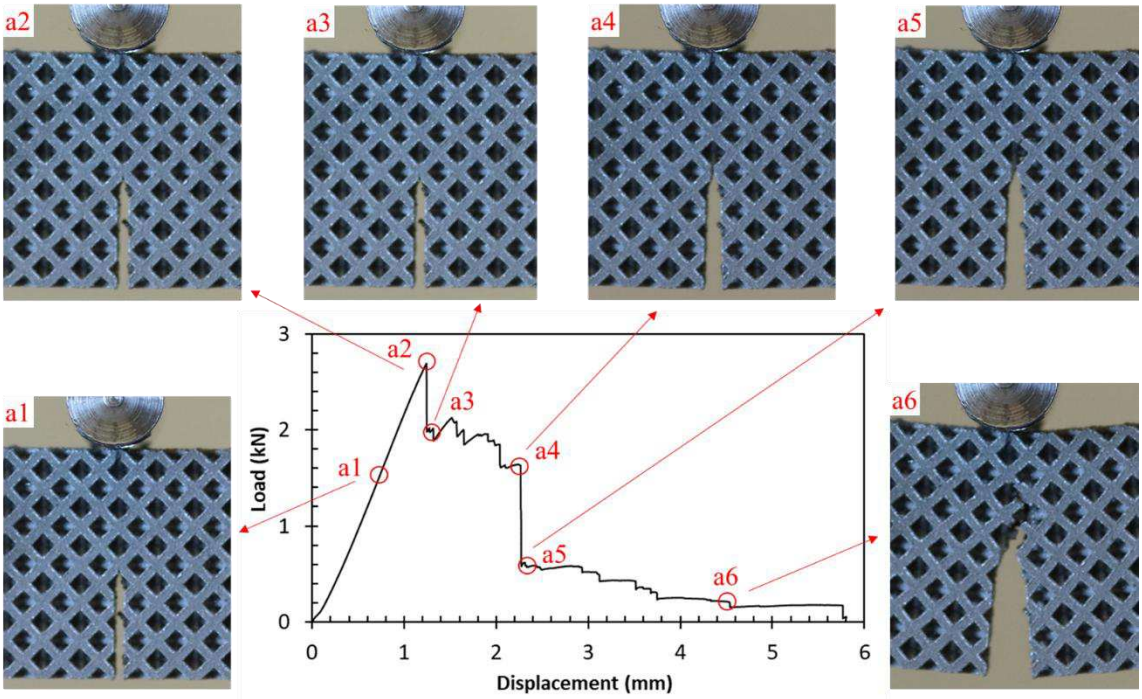


Fig. 5. Photographs taken for a chosen specimen (sample 1) during mode I testing at different deformation stages.

4.2. Numerical results

4.2.1. Calibrated material properties

In the numerical study, the calibration was performed such that the initial material properties of Ti6Al4V [50] given in Table 2 were reduced by some factors by following the flowchart in Fig. 4. The comparison between the peak load and stiffness values of the numerical and experimental load-displacement responses were compared and the properties were updated until the differences were respectively lower than 3% and 8% for accepting updated material properties as the calibrated ones. The obtained data during some steps of the calibration process are listed in Table 4. The symbol RF signifies the reduction value, which was multiplied by the initial (reference) values of Ti-6Al-4V material properties in each step. The last line of the table indicates the calibrated material properties used in the XFEM analyses using the ESMM. During the initial steps shown in Table 4, by comparing the average experimental values (2746.67 N and 2459.67 N/mm for the peak load and stiffness) with the corresponding numerical ones, it was understood that the material properties should be reduced significantly. This reduction in the third step was applied only on Young's modulus and ultimate strength, whereas after steps 5 and 6, only Young's modulus was reduced to obtain accurate results,

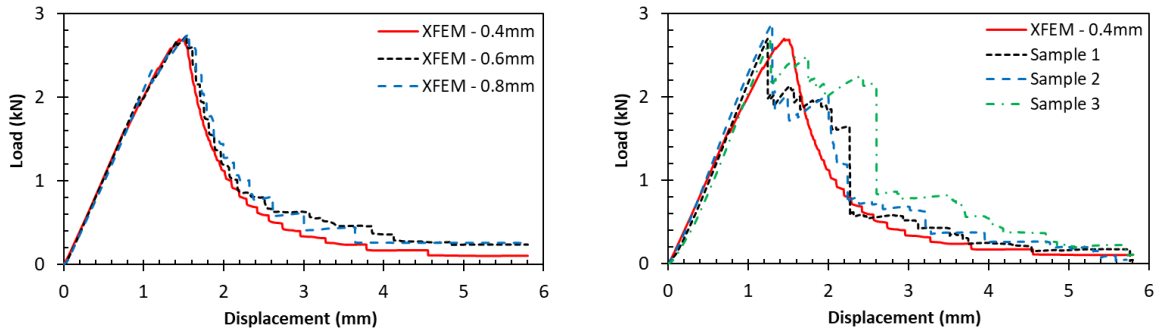
followed by another reduction imposed only on ultimate strength at step 7. The reduction of only fracture toughness was performed at step 8. To guarantee the exactness of the results, one more reduction was imposed on Young's modulus, ultimate strength, and fracture toughness values one by one during steps 9 to 11, respectively. At the last step, a difference value of 2.2% and 7.9% was attained between the numerical and experimental values of the peak load and stiffness, respectively. Thus, the calibration process was truncated when the discrepancy was reduced below the acceptance limits. The load-displacement response of numerical analysis with the calibrated material properties is shown in Fig. 6(a) for different element sizes.

Table 4. The updated material properties obtained during some selected steps of the calibration process for the lattice structure. The relative percentage differences were compared to the average experimental values (2746.67 N and 2459.67 N/mm for the peak load and stiffness).

Step	E (GPa)		σ_u (MPa)		K_I (MPa$\sqrt{m}$)		Difference = 100*(Exp. - Num.)/(Exp.)	
	Value	**RF**	**Value**	**RF**	**Value**	**RF**	**Peak load difference (%)**	**Stiffness difference (%)**
0 (Initial) [50]	117	-	1140	-	45	-	242.8	1034.1
1	70.2	0.6	684	0.6	27	0.6	107.3	588.6
2	64.35	0.55	627	0.55	24.75	0.55	69.6	476.1
3	40.95	0.35	399	0.35	24.75	0.55	42.7	287.0
4	29.25	0.25	285	0.25	24.75	0.55	39.8	189.5
5	17.55	0.15	285	0.25	24.75	0.55	39.6	88.1
6	11.7	0.10	285	0.25	24.75	0.55	39.3	15.4
7	11.7	0.10	250.8	0.22	24.75	0.55	36.7	15.3
8	11.7	0.10	250.8	0.22	16.2	0.36	2.9	15.6
9	9	0.077	250.8	0.22	16.2	0.36	2.8	11.2
10	9	0.077	240	0.211	16.2	0.36	2.3	11.1
11 (Calibrated)	**9**	0.077	**240**	0.211	**16**	0.355	2.2	7.9

4.2.2. Mesh refinement study

A mesh refinement study was performed using the calibrated material properties, and for three different element sizes, including 0.8, 0.6, and 0.4 mm. The results are shown in Fig. 6(a). Considering the computational costs and the difference between the load-displacement responses of different element sizes, it was revealed that a mesh size of 0.4 mm reflected suitable results. A comparison between the experimental results and numerical ones obtained using an element size of 0.4 was conducted, as shown in Fig. 6(b).



(a) **(b)**

Fig. 6. Numerical load-displacement responses of the SENB lattice specimen: (a) of different element sizes and (b) compared to the experimental ones.

The figure demonstrates the suitability of the numerical results obtained using the calibrated material properties (Table 4) and an element size of 0.4 mm. The numerical and experimental results are compared in Table 5.

Table 5. Comparison between experimental and numerical results after the calibration of material properties and mesh refinement study.

Experimental Data		**Numerical Data** (Element Size=0.4 mm)		**Difference [%]**	
Average Peak Load [N]	**Average Stiffness [N/mm]**	**Peak Load [N]**	**Stiffness [N/mm]**	**Peak Load [%]**	**Stiffness [%]**
2746.67	2459.67	2687	2265	2.2	7.9

4.2.3. Fracture and crack propagation

The crack propagation in the XFEM analysis of the equivalent solid model of the FSCC lattice specimen is shown in Fig. 7. Since the element size is small (i.e., 0.4 mm), a detailed section around the crack tip is also shown in the figure. The elements in front of the crack tip were split up into two pieces as per expectations acquired from the experimental observations shown in Fig. 5. Since the equivalent solid model has been created from the solid homogeneous elements, the crack grows upward vertically. However, there is a deviation in the crack propagation path in the experimental observation, which can be justified by the nature of the lattice structure. As later shown in Fig. 8, the fracture surface is not smooth, considering the presentation of struts in both horizontal and vertical orientations in front of the crack propagation path.

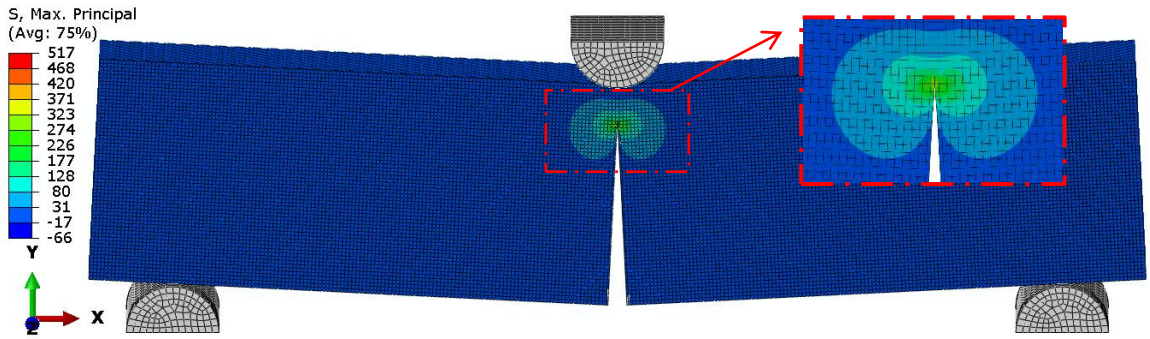


Fig. 7. Crack propagation in the XFEM analysis of the equivalent solid model using an element size of 0.4 mm.

4.3. Fracture surfaces

4.3.1. Photography investigations

Fracture surface investigation was initially conducted using high precision photography using a using a Macro Lens (RF 100mm F2.8L Macro IS USM) mounted on a Canon camera. Fig. 8 indicates the fracture surfaces of the specimens tested under 3P-bending loading. It is clear that the fracture surfaces are not smooth and completely planar despite the fact that the crack growth is expected to be vertical considering the nature of 3P-bending mode I loading. This can be justified by the fact that there are both horizontal and vertical struts in front of the crack propagating in FSCC SENB specimens [36]. In other words, the presence of struts in both vertical and horizontal orientations cause the fracture surface to be of several fluctuations.

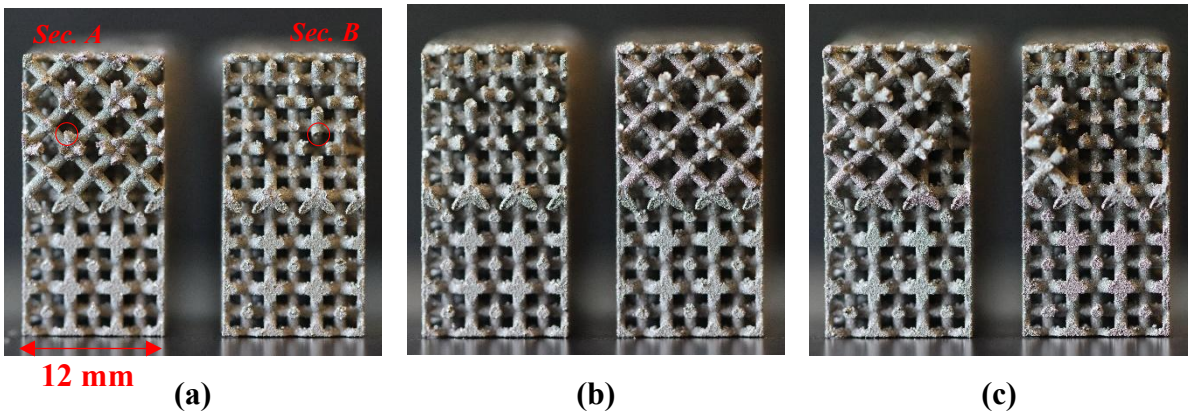
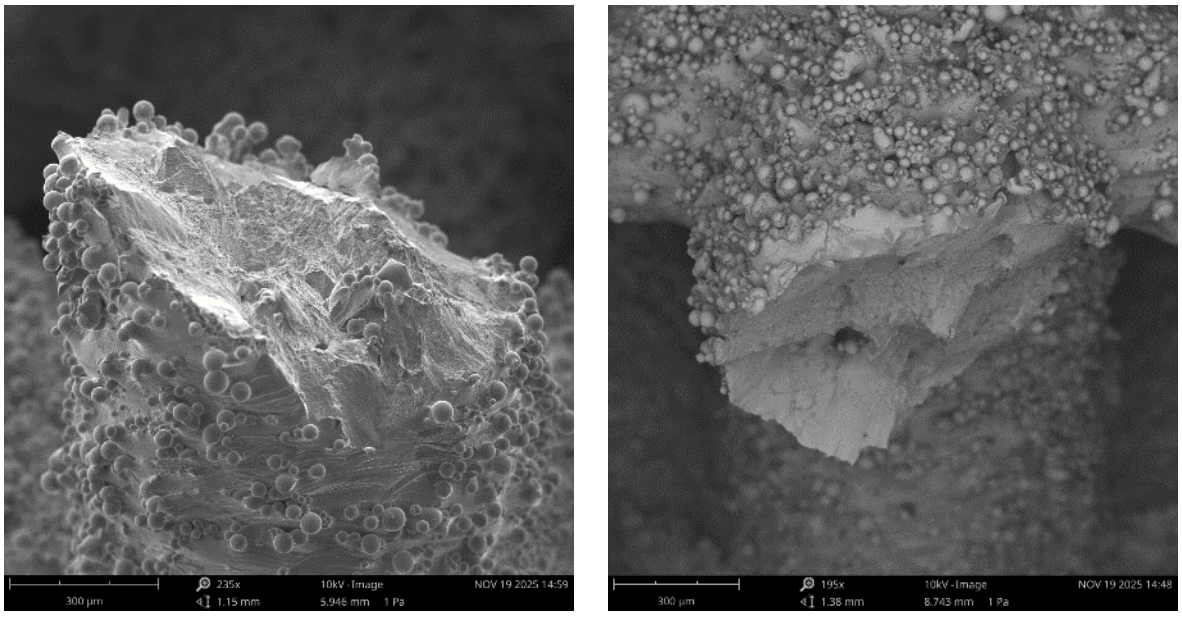


Fig. 8. Fracture surfaces of tested lattice specimens (photographs were taken using a Macro Lens (RF 100mm F2.8L Macro IS USM) mounted on a Canon camera) (a) Sample 1, (b) Sample 2, and (c) Sample 3.

4.3.2. SEM investigations

SEM investigations of the fracture surfaces were performed in order to observe the fracture plane at the struts after failure using a Phenom XL scanning electron microscope (Thermo Fisher Scientific). Imaging was conducted in high-vacuum mode at an accelerating voltage of 10 kV, with a working distance of approximately 8 mm. SEM images were taken for one specimen after failure. Each pair of fracture samples was cut into a suitable size to take SEM images. Both corresponding fracture surfaces (i.e., both fracture surfaces created after fracture of the selected strut) were put next to each other while taking SEM images for comparison purposes. The images shown in Fig. 9 are related to the locations indicated in red in Fig. 8(a). It shows the generation of several small crack planes on the fracture surface of a selected strut. The creation of several crack planes on the fracture surface can justify the fluctuations experienced in the load-displacement response of the corresponding specimen. This type of fracture, reflecting the brittle cleavage fracture, has also been investigated by Parameswaran et al. [51] for Ti6Al4V lattice structures. Additionally, as shown in the figure, at this macroscale, the fracture surfaces of the struts appear relatively planar with limited evidence of extensive plastic deformation. The presence of partially fused or unmelted powder particles attached to the surface is typical of the as-built L-PBF condition [52].



(a) **(b)**

Fig. 9. The SEM images taken from the fracture surfaces. Both sides of a strut after failure: (a) *Sec. A* at Fig. 8 and (b) *Sec. B* at Fig. 8.

5. Conclusions

This research experimentally and numerically investigated the mode I fracture behavior of Ti-6Al-4V FSCC lattice specimens fabricated by PBF-LB/M technique. To overcome the computational expense of modeling the complex lattice structure, an ESMM approach was calibrated to extract the effective mechanical and fracture properties of the FSCC lattice, facilitating efficient XFEM analyses of the lattice specimens.

The calibrated material properties reflected appropriate numerical results with acceptable differences from experimental results: 2.2% and 7.9% differences for the peak load and stiffness values, respectively. The XFEM simulations utilizing the ESMM approach predicted a perfectly vertical crack propagation path characteristic of mode I loading, while the experimental lattice specimens exhibited localized fluctuations and crack path deviations. These deviations demonstrated that the physical crack-deflection mechanisms induced by the central vertical and horizontal struts, highlighting the enhanced damage tolerance inherent to the near-isotropic architecture of the FSCC cell.

The accurate numerical predictability and consistent fracture resistance observed in the Ti-6Al-4V FSCC lattice specimens underscore its significant potential for advanced engineering applications subjected to complex, multidirectional loading environments. Future work will focus on integrating these near-isotropic lattices into the design of damage-tolerant aerospace joint nodes and customized biomedical implants. Additionally, further experimental and numerical investigations into the Mode II, Mode III, and mixed-mode fracture behavior of the FSCC lattice will be essential to fully characterize its damage tolerance and failure mechanisms under real-world, multidirectional loading conditions.

Authors' Contributions: B.P.: Conceptualization; investigation; methodology; data curation; formal analysis; visualization; validation; writing—original draft. R.M.G.: Conceptualization; investigation; supervision; funding acquisition; project administration; resources; writing—review and editing. N.B.: Investigation; resources; writing—review and editing.

Supplementary Materials: The online version contains one Supplementary File.

Conflict of Interest: On behalf of all authors, the corresponding author declares that no known competing financial interests or personal relationships could have appeared to influence the work reported in this paper.

Data availability: The datasets generated during and/or analyzed during the current study are available from the corresponding author upon reasonable request.

Acknowledgment: The authors would like to thank Muhammed Taha Yildiz from Sivas University of Science and Technology for fabricating the L-PBF specimens.

References:

1. Gergely, V. and B. Clyne, *The FORMGRIP Process: Foaming of Reinforced Metals by Gas Release in Precursors.* Advanced Engineering Materials, 2000. **2**(4): p. 175-178.
2. Boyer, R.R., *An overview on the use of titanium in the aerospace industry.* Materials Science and Engineering: A, 1996. **213**(1): p. 103-114.
3. Kuziak, R., R. Kawalla, and S. Waengler, *Advanced high strength steels for automotive industry.* Archives of Civil and Mechanical Engineering, 2008. **8**(2): p. 103-117.
4. Gibson, I., et al., *Development of Additive Manufacturing Technology*, in *Additive Manufacturing Technologies*, I. Gibson, et al., Editors. 2021, Springer International Publishing: Cham. p. 23-51.
5. Yan, C., et al., *Evaluations of cellular lattice structures manufactured using selective laser melting.* International Journal of Machine Tools and Manufacture, 2012. **62**: p. 32-38.
6. Osakada, K. and M. Shiomi, *Flexible manufacturing of metallic products by selective laser melting of powder.* International Journal of Machine Tools and Manufacture, 2006. **46**(11): p. 1188-1193.
7. Gokuldoss, P.K., *Selective Laser Melting: Materials and Applications*. 2020: MDPI AG.
8. Yap, C.Y., et al., *Review of selective laser melting: Materials and applications.* Applied Physics Reviews, 2015. **2**(4).
9. Shishkovsky, I., *New Trends in 3D Printing*. 2016: IntechOpen.
10. Mazur, M., et al., *Deformation and failure behaviour of Ti-6Al-4V lattice structures manufactured by selective laser melting (SLM).* The International Journal of Advanced Manufacturing Technology, 2016. **84**(5): p. 1391-1411.
11. Luo, Y., et al., *Microstructure and Mechanical Properties of Ti-6Al-4V Rods Fabricated by Powder Compact Extrusion of TiH2/Al60V40 Powder Blend.* Metallurgical and Materials Transactions A, 2019. **50**(4): p. 1643-1654.
12. Zhu, Q., et al., *Effect of solution treatments on microstructure and mechanical properties of Ti–6Al–4V alloy hot rolled sheet.* Journal of Materials Research and Technology, 2023. **23**: p. 5760-5771.
13. Fan, G. and L. Gao, *Mechanical property of Ti-6Al-4V sheet in one-sided electric hot incremental forming.* The International Journal of Advanced Manufacturing Technology, 2014. **72**(5): p. 989-994.
14. Bai, L., et al., *Heterogeneous compressive responses of additively manufactured Ti-6Al-4V lattice structures by varying geometric parameters of cells.* International Journal of Mechanical Sciences, 2022. **214**: p. 106922.

15. Lu, S.L., et al., *Microstructure and Mechanical Properties of Long Ti-6Al-4V Rods Additively Manufactured by Selective Electron Beam Melting Out of a Deep Powder Bed and the Effect of Subsequent Hot Isostatic Pressing.* Metallurgical and Materials Transactions A, 2015. **46**(9): p. 3824-3834.
16. Wauthle, R., et al., *Effects of build orientation and heat treatment on the microstructure and mechanical properties of selective laser melted Ti6Al4V lattice structures.* Additive Manufacturing, 2015. **5**: p. 77-84.
17. Ramadani, R., et al. *Selective Laser Melting of a Ti-6Al-4V Lattice-Structure Gear: Design, Topology Optimization, and Experimental Validation*. Applied Sciences, 2025. **15**, 7949 DOI: 10.3390/app15147949.
18. Cooper, D., et al., *Design and manufacture of high performance hollow engine valves by Additive Layer Manufacturing.* Materials & Design, 2015. **69**: p. 44-55.
19. Brandt, M., et al., *High-Value SLM Aerospace Components: From Design to Manufacture.* Advanced Materials Research, 2013. **633**: p. 135-147.
20. Huang, M., et al., *Damage modes and mechanical properties of Ti6Al4V lattice structures under transverse impact loading.* Additive Manufacturing Letters, 2025. **14**: p. 100294.
21. Kumawat, S., S.R. Deshmukh, and R.R. Ghorpade, *Fabrication of Ti-6Al-4v cellular lattice structure using selective laser melting for orthopedic use: A review.* Materials Today: Proceedings, 2024. **113**: p. 166-172.
22. Campoli, G., et al., *Mechanical properties of open-cell metallic biomaterials manufactured using additive manufacturing.* Materials & Design, 2013. **49**: p. 957-965.
23. Babaee, S., et al., *Mechanical properties of open-cell rhombic dodecahedron cellular structures.* Acta Materialia, 2012. **60**(6): p. 2873-2885.
24. Hedayati, R., et al., *Comparison of elastic properties of open-cell metallic biomaterials with different unit cell types.* Journal of Biomedical Materials Research Part B: Applied Biomaterials, 2018. **106**(1): p. 386-398.
25. Maskery, I., et al., *A mechanical property evaluation of graded density Al-Si10-Mg lattice structures manufactured by selective laser melting.* Materials Science and Engineering: A, 2016. **670**: p. 264-274.
26. Smith, M., Z. Guan, and W.J. Cantwell, *Finite element modelling of the compressive response of lattice structures manufactured using the selective laser melting technique.* International Journal of Mechanical Sciences, 2013. **67**: p. 28-41.
27. Xiao, L. and W. Song, *Additively-manufactured functionally graded Ti-6Al-4V lattice structures with high strength under static and dynamic loading: Experiments.* International Journal of Impact Engineering, 2018. **111**: p. 255-272.
28. Xiao, L., et al., *Mechanical properties of open-cell rhombic dodecahedron titanium alloy lattice structure manufactured using electron beam melting under dynamic loading.* International Journal of Impact Engineering, 2017. **100**: p. 75-89.
29. Ozdemir, Z., et al., *Energy absorption in lattice structures in dynamics: Experiments.* International Journal of Impact Engineering, 2016. **89**: p. 49-61.
30. Leuders, S., et al., *On the mechanical behaviour of titanium alloy TiAl6V4 manufactured by selective laser melting: Fatigue resistance and crack growth performance.* International Journal of Fatigue, 2013. **48**: p. 300-307.
31. Hedayati, R., et al., *Computational prediction of the fatigue behavior of additively manufactured porous metallic biomaterials.* International Journal of Fatigue, 2016. **84**: p. 67-79.
32. Horn, T.J., et al., *Flexural properties of Ti6Al4V rhombic dodecahedron open cellular structures fabricated with electron beam melting.* Additive Manufacturing, 2014. **1-4**: p. 2-11.
33. Demirtunç, M. and R.M. Gorguluarslan, *Elastically near-isotropic equal-diameter lattice material for topology optimization and additive manufacturing.* Composite Structures, 2026. **383**: p. 120136.

34. Li, X., et al., *Heterogeneously tempered martensitic high strength steel by selective laser melting and its micro-lattice: Processing, microstructure, superior performance and mechanisms.* Materials & Design, 2019. **178**: p. 107881.
35. Paygozar, B., *Investigation of mechanical and fracture behaviors of additively manufactured polymeric lattice materials*. 2025, PhD Thesis, Mechanical Engineering, TOBB University of Economics and Technology.
36. Paygozar, B. and R.M. Gorguluarslan, *Experimental investigation of build orientation effects on mechanical and fracture behaviors of additively manufactured lattice materials.* Mechanics of Advanced Materials and Structures, 2026. **33**(1): p. 2625365.
37. Daynes, S., et al., *Fracture toughness characteristics of additively manufactured Ti–6Al–4V lattices.* European Journal of Mechanics - A/Solids, 2021. **86**: p. 104170.
38. Al-wattar, T.A.A., *Developing equivalent solid model for lattice cell structure using numerical approaches.* 2020.
39. Alwattar, T.A. and A. Mian *Developing an Equivalent Solid Material Model for BCC Lattice Cell Structures Involving Vertical and Horizontal Struts*. Journal of Composites Science, 2020. **4**, DOI: 10.3390/jcs4020074.
40. Ghandriz, R., K. Hart, and J. Li, *Extended finite element method (XFEM) modeling of fracture in additively manufactured polymers.* Additive Manufacturing, 2020. **31**: p. 100945.
41. Akhavan-Safar, A., et al., *Mixed mode I/III fracture behavior of adhesive joints.* International Journal of Solids and Structures, 2020. **199**: p. 109-119.
42. Mubashar, A., I.A. Ashcroft, and A.D. Crocombe, *Modelling Damage and Failure in Adhesive Joints Using A Combined XFEM-Cohesive Element Methodology.* The Journal of Adhesion, 2014. **90**(8): p. 682-697.
43. Stein, N., et al., *Enhanced XFEM for crack deflection in multi-material joints.* International Journal of Fracture, 2017. **207**(2): p. 193-210.
44. Biswakarma, J.J.S., et al., *Modeling Brittle Fractures in Epoxy Nanocomposites Using Extended Finite Element and Cohesive Zone Surface Methods.* Polymers, 2021. **13**(19): p. 3387.
45. Giner, E., et al., *An Abaqus implementation of the extended finite element method.* Engineering Fracture Mechanics, 2009. **76**(3): p. 347-368.
46. Paygozar, B. and R.M. Gorguluarslan, *Investigating Failure Behavior of Adhesive Joints with Dissimilar Materials of Steel and Additively Manufactured PLA.* Transactions of the Indian Institute of Metals, 2023. **76**(11): p. 3041-3048.
47. Elices, M., et al., *The cohesive zone model: advantages, limitations and challenges.* Engineering Fracture Mechanics, 2002. **69**(2): p. 137-163.
48. Campilho, R.D.S.G., et al., *eXtended Finite Element Method for fracture characterization of adhesive joints in pure mode I.* Computational Materials Science, 2011. **50**(4): p. 1543-1549.
49. Paygozar, B., et al., *Adhesively bonded aluminium double-strap joints: effects of patch part on failure load.* Journal of the Brazilian Society of Mechanical Sciences and Engineering, 2020. **42**(11): p. 589.
50. Louw, D.F., et al., *Fracture toughness of laser-based powder bed fusion produced Ti-6Al-4V.* Materials Science and Engineering: A, 2025. **931**: p. 148199.
51. Parameswaran, P., et al., *A Study on Compression Behavior and Fracture Morphology in Dumbbell-Shaped Ti6Al4V Lattice Structures Fabricated through Additive Manufacturing.* Journal of Materials Engineering and Performance, 2025. **34**(17): p. 18738-18753.
52. Seremet, H. and N. Babacan, *Compressive properties of AlSi10Mg lattice structures with novel BCCZZ and FCCZZ configurations fabricated by selective laser melting.* Rapid Prototyping Journal, 2024. **30**(4): p. 770-781.

Supplementary Files

This is a list of supplementary files associated with this preprint. Click to download.

- S1.SupplementaryFile1.docx